Journal of Computational and Applied Mechanics, Vol. 20, No. 2, (2025), pp. 71–92
DOI: 10.32973/jcam.2025.003

INITIAL STATE DEPENDENCE OF THERMO-MECHANICAL COUPLING IN HEAT CONDUCTION NEAR THE LIQUID-VAPOR CRITICAL POINT

Kristóf Tóth
Department of Energy Engineering, Faculty of Mechanical Engineering,
Budapest University of Technology and Economics
Műegyetem rkp. 3., H-1111 Budapest, Hungary
kristofferenctoth@edu.bme.hu

Mátyás Szücs
Department of Energy Engineering, Faculty of Mechanical Engineering,
Budapest University of Technology and Economics
Műegyetem rkp. 3., H-1111 Budapest, Hungary;
Institute for Particle and Nuclear Physics, HUN-REN Wigner Research Centre for Physics
Konkoly-Thege Miklós út 29–33, H-1121 Budapest, Hungary;
Montavid Thermodynamic Research Group,
Society for the Unity of Science and Technology
Lovas út 18., H-1012 Budapest, Hungary
szucs.matyas@gpk.bme.hu

[Received: December 13, 2025; Accepted: February 23, 2026]

Abstract. In the vicinity of the liquid–vapor critical point, fluids behave in a strongly compressible manner and their thermophysical parameters exhibit significant state-dependence, leading to an intense coupling of the mechanical and the thermal processes. For instance, the piston effect is a coupled thermo-acoustic phenomenon when close to a heated surface a thermal boundary layer forms in the fluid, which expands due to the relatively large value of the isobaric thermal expansion coefficient. Accordingly, the expansion of the boundary layer caused by its temperature change excites pressure waves in the fluid, which also transports thermal energy during its propagation. Therefore, the propagation of the temperature at the speed of sound can be observed, in contrast to the delayed nature of the diffusive heat propagation. In this study, an effective heat conduction model is investigated in the linear approximation, which neglects acoustic propagation, but considers the effect of thermal expansion. We identify and analyze the state-dependent parameters influencing the dynamics and explore through numerical simulations how the initial conditions affect the process .

Mathematical Subject Classification: 76N06, 80M20
Keywords: supercritical fluids, heat conduction, thermal expansion, coupled problems, piston effect, finite difference method

1. Introduction

Liquids and gases can only be distinguished within a limited region of the thermodynamic state space. The coexistence curve terminates at the liquid-vapor critical point, where the thermophysical properties of the two phases become increasingly

similar. In the critical point, phase boundaries vanish; thus, the heat of vaporization approaches zero. The critical point is a material-specific property defined by its temperature, pressure, and density. Above a critical temperature and pressure, the fluid exhibits both liquid and gas characteristics, allowing continuous transformation between these states without a phase transition [1].

In the vicinity of the critical point, the fluid becomes strongly compressible and in parallel, its thermophysical properties exhibit rapid changes, even by orders of magnitude [2, 3]. Although the design of systems operating with supercritical fluids is complicated by anomalies in the material properties and corrosion risks, the advantages of supercritical fluids are widely exploited in industrial and energy applications. For instance, in the food and pharmaceutical industries, supercritical carbon dioxide extraction is used for decaffeination, aroma recovery, and sterilization processes, taking advantage of the fluid's excellent solvability and diffusion characteristics [4]. In the energy sector, supercritical steam cycles and fourth-generation nuclear reactors employing supercritical coolants enable significant efficiency improvements, while supercritical carbon dioxide based power systems offer compact turbine and heat exchanger solutions [5, 6]. Furthermore, the usage of supercritical carbon dioxide offers new perspectives for enhanced geothermal systems to extract heat from hot dry rocks [7, 8]. This technology may also be integrated in carbon sequestration strategies. Since differences between liquid and gas vanish in supercritical states, phenomena such as boiling crisis can be avoided; however, other technical difficulties may occur, such as heat transfer deterioration [9]. Therefore, the proper design and safe operation of supercritical systems require a thorough understanding of the coupled thermomechanical phenomena that emerge in supercritical fluids.

Near the critical point, the compressibility and the state dependence of the material parameters result in the coupling of thermal and flow processes [10, 11]. Consider a tank filled with a fluid near its critical point. When the wall of the tank is heated, a thermal boundary layer forms near the heated surface and expands due to the relatively large thermal expansion coefficient, while the expanding boundary layer compresses the bulk fluid like a piston. This phenomenon, known as the *piston effect*, results in an almost isentropic pressure rise, which leads to a rapid temperature increase in the bulk, contrasting with the slow nature of the diffusive heat transfer. Consequently, heat conduction is significantly influenced by thermal expansion.

Although previous works (*e.g.,* [12–14]) thoroughly analyze thermo-mechanical coupling and the piston effect, these studies generally consider a fixed initial thermodynamic state; hence, the sensitivity of the phenomenon to slight variations in the initial temperature or pressure has not been explicitly analyzed. While the experimental investigations carried out during the SpaceLab D2 mission [15] explored the piston effect at several initial temperatures, the focus was the empirical confirmation of fast temperature propagation rather than a systematic characterization of the initial-state dependence. In this work, we investigate the dependence of the piston effect on the initial thermodynamic state. Although our analysis relies on linearized equations, the intense variations in the material properties near the critical point lead to unexpected behavior. We identify the parameters governing the dynamics, thereby explaining why

processes initiated under nearly identical conditions may exhibit significantly different transients. These findings are also corroborated through numerical simulations. In summary, the present study clarifies and quantifies the role of the initial state in the dynamics of the piston effect.

Our long-term goal is to investigate the effect of material nonlinearities on heat conduction near the critical point. This work also serves as a preliminary study for this future investigation and as a preparation for the numerical methodology required for the analysis of nonlinear behavior.

The first results have been presented at the Student's Scientific Conference at Budapest University of Technology and Economics by Kristóf Tóth with the supervision of Mátyás Szücs [16]. Here we present a more systematic background for the phenomenon and an extended analysis of the material behavior near the critical point.

2. The piston effect

Anomalies of material properties near the critical point lead to peculiar heat transfer phenomena. Usually, heat conduction in a medium which is at rest with respect to an inertial reference system is described via the heat equation

$$\varrho c_p \frac{\partial T}{\partial t} = \nabla \cdot (\lambda \nabla T)\,, \tag{2.1}$$

where T is the temperature field (*i.e.,* a time and space dependent function), ϱ, c_p and λ are the density, the isobaric specific heat capacity and the thermal conductivity, respectively, $\frac{\partial}{\partial t}$ is the partial time derivative and ∇ is the nabla operator, which – depending on the vectorial multiplication – denotes the gradient or divergence. Assuming constant thermophysical parameters, (2.1) can be reformulated to

$$\frac{\partial T}{\partial t} = \alpha \nabla^2 T \tag{2.2}$$

with the thermal diffusivity $\alpha = \frac{\lambda}{\varrho c_p}$ and the Laplace operator ∇^2. By introducing a characteristic length scale ℓ, the *thermal diffusion time scale* can be defined as

$$t_\mathrm{d} = \frac{\ell^2}{\alpha}, \tag{2.3}$$

which characterizes diffusive propagation. At the critical point, the isobaric specific heat capacity diverges, thus thermal diffusivity tends to zero. Figure 1 presents the state dependence of the thermal diffusivity of carbon dioxide, calculated from the Span–Wagner equation of state [17] together with the reference thermal-conductivity correlation [18]. Consequently, near the critical point, heat conduction is expected to decelerate drastically, which is referred to in the literature as 'critical slowing down' [10, 11].

In contrast, experiments conducted under terrestrial conditions have shown rapid temperature homogenization in supercritical fluids, which contradicts the previous theoretical prediction. This observation was explained by convective mixing caused by buoyancy, but in a space experiment, the same rapid temperature homogenization

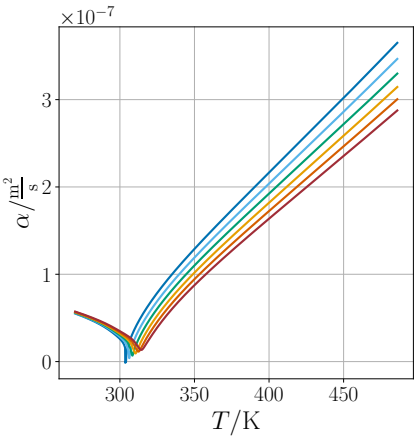

Figure 1. Temperature dependence of the thermal diffusivity of carbon dioxide along the isobaric lines $\approx 1p_c$, $1.05p_c$, $1.1p_c$, $1.15p_c$, $1.2p_c$ and $1.25p_c$ (from dark blue to red, respectively). Critical temperature and pressure of carbon dioxide are $T_c = 304.1282$ K and $p_c = 7.3773$ MPa.

was observed in the absence of gravity, similar to measurements performed on Earth. This phenomenon is often referred to in the literature as 'critical speeding up' [12–14].

This observation is explained by the coupling of the thermal and the mechanical processes caused by thermal expansion. Since heat conduction is slow near the critical point, a thin thermal boundary layer forms in the fluid near the heated surfaces. Due to the large value of the isobaric thermal expansion coefficient, the fluid elements forming the boundary layer expand, thus inducing density and pressure variations. These disturbances propagate adiabatically through the fluid at the speed of sound [19, 20]. Consequently, the propagation of temperature at the speed of sound can also be observed, described by the acoustic wave equation

$$\frac{\partial^2 T}{\partial t^2} = a_s^2 \nabla^2 T \tag{2.4}$$

with a_s denoting the isentropic speed of sound. The acoustic propagation is characterized by the *acoustic time scale*

$$t_a = \frac{\ell}{a_s}. \tag{2.5}$$

At the critical point, the isentropic speed of sound tends to zero (for carbon dioxide calculated from the Span–Wagner equation of state [17], see the left-hand diagram of Figure 2), similarly to the thermal diffusivity. At first, it may seem paradoxical that acoustic propagation, which is considered a fundamentally fast process, also slows down in the vicinity of the critical point. However, compared to the diffusion time

scale, one can say that acoustic processes are fast if $t_\mathrm{a} \ll t_\mathrm{d}$, which is fulfilled if

$$\frac{\alpha}{a_s} \ll \ell \tag{2.6}$$

holds. As shown in the right-hand diagram of Figure 2 for carbon dioxide, the previously identified material-specific characteristic length scale $\frac{\alpha}{a_s}$ is on the order of 10^{-9} m.

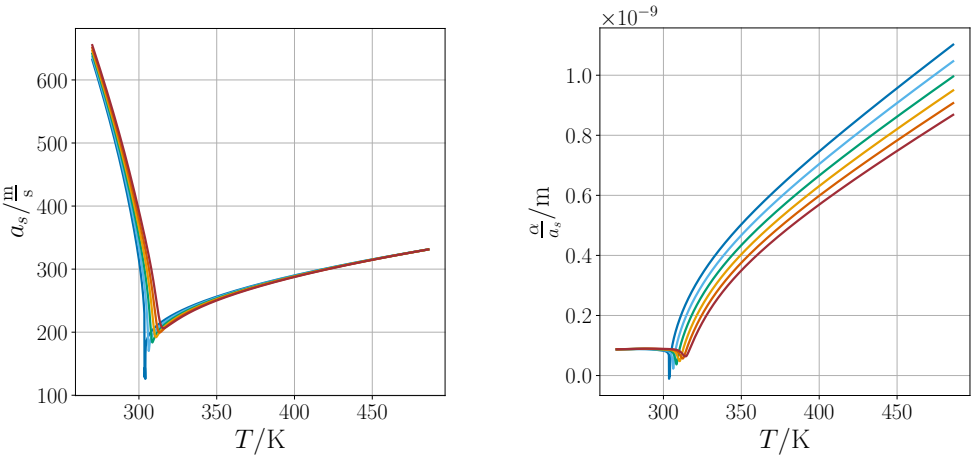

Figure 2. Temperature dependence of the isentropic speed of sound of carbon dioxide (*left*) and the material originated characteristic length scale $\frac{\alpha}{a_s}$ (*right*) along the isobaric lines $\approx 1p_\mathrm{c}$, $1.05p_\mathrm{c}$, $1.1p_\mathrm{c}$, $1.15p_\mathrm{c}$, $1.2p_\mathrm{c}$ and $1.25p_\mathrm{c}$ (from dark blue to red, respectively).

In light of our previous statements, the temperature change in a supercritical fluid can be observed practically immediately in the centimeter-sized samples used in experiments. For example, during the SpaceLab D2 mission, a series of experiments were conducted to verify the piston effect [15]. A thin-walled, spherical tank made of copper was filled with sulfur hexafluoride in a state close to its critical point. Due to the excellent thermal conductivity of copper, a homogeneous temperature rise was created on the fluid interface by heating the tank wall along a single equator with a heating filament. By ensuring spherical symmetry, the experiment could be evaluated in a single spatial dimension: temperature in the fluid was measured with thermistors at three points along the radial direction. In the experiments a heat-pulse-type excitation was applied, which means that the duration of surface heating t_p is much smaller than the diffusion time scale. However, from a technological point of view, to deliver a sufficient amount of heat, this heating time must be much longer than the acoustic time scale. This results in the suppression of acoustic processes, *i.e.,* pressure increases during the heating phase and correspondingly, the nearly isentropic temperature rise caused by the expansion of the thermal boundary layer seemingly occurs immediately without delay, implying a nearly homogeneous temperature change in

the bulk fluid. These experiments reliably confirmed the piston effect in supercritical fluids.

Although our previous argumentation essentially explains the coupling of the thermal and the mechanical processes in supercritical fluids, the usual form of the heat equation (2.2) is unable to describe such processes. Therefore, in the next subsection we briefly summarize the governing equations of coupled thermomechanical processes of fluids.

2.1. **Thermomechanical processes of fluids.** The first law of thermodynamics for a fluid element can be formulated as

$$\varrho c_p \dot{T} = -\nabla \cdot \mathbf{J}_Q + T\beta_p \dot{p} - \mathbf{\Pi} : \nabla \mathbf{v}^{\mathrm{Sym}}, \tag{2.7}$$

where ϱ, $\mathbf{v}$, $\mathbf{J}_Q$, p and $\mathbf{\Pi}$ are the density, the velocity, the heat current density, the (hydrostatic) pressure and the viscous pressure tensor, respectively [21, 22]. Furthermore, $^{\mathrm{Sym}}$ denotes the symmetric part of a second-order tensor, while the double dot product is a contraction over both indices, *i.e.,* for the tensors $\mathbf{A}$ and $\mathbf{B}$ it is defined as $\mathbf{A} : \mathbf{B} = \mathrm{tr}\left(\mathbf{A}^{\mathrm{T}}\mathbf{B}\right)$, with $^{\mathrm{T}}$ denoting the transpose and tr denoting the trace. The material time derivative

$$\dot{T} = \left(\frac{\partial}{\partial t} + \mathbf{v} \cdot \nabla\right) T \tag{2.8}$$

describes how the temperature field (as well as the pressure field) in a fixed material point changes in time, while it travels at velocity $\mathbf{v}$. Thermostatic material properties are defined by the partial derivatives of the thermal and the caloric state functions, $\varrho(T, p)$ and $h(T, p)$, respectively, with h denoting the specific enthalpy. Correspondingly, the isobaric volumetric thermal expansion coefficient β_p, the isothermal compressibility χ_T and the isobaric specific heat capacity c_p are

$$\beta_p = -\frac{1}{\varrho}\left.\frac{\partial \varrho}{\partial T}\right|_p, \qquad \chi_T = \frac{1}{\varrho}\left.\frac{\partial \varrho}{\partial p}\right|_T, \qquad c_p = \left.\frac{\partial h}{\partial T}\right|_p, \tag{2.9}$$

respectively. Thermodynamic compatibility of the thermal and the caloric equations of state is ensured through the specific entropy: when three material properties are known, then the fluid is fully characterized from a thermomechanical point of view. Thus, material properties that often arise in practical applications can be formulated as follows:

- isochoric specific heat capacity: $$c_v = c_p - \frac{T}{\varrho}\frac{\beta_p^2}{\chi_T}, \tag{2.10}$$
- heat capacity ratio: $$\gamma = \frac{c_p}{c_v} = 1 + \frac{T}{\varrho}\frac{\beta_p^2}{c_v \chi_T}, \tag{2.11}$$
- isentropic speed of sound: $$a_s = \sqrt{\frac{\gamma}{\varrho \chi_T}}. \tag{2.12}$$

Let us note here that heat capacity ratio creates further relationships, namely between the isothermal and the isentropic compressibility, as well as the isentropic and the

isothermal speed of sound, *i.e.,* $\gamma = \frac{\chi_T}{\chi_s} = \frac{a_s^2}{a_T^2}$. Internal stability of the material is ensured by the positivity of c_v and χ_T [23–25].

Usually, the heat current density and the viscous pressure are characterized by Fourier's heat conduction law and Newton's viscosity law, *i.e.,*

$$\mathbf{J}_Q = -\lambda \nabla T, \tag{2.13}$$

$$\mathbf{\Pi} = -\left(\eta_{\mathrm{Vol}} - \frac{2}{3}\eta\right)(\nabla \cdot \mathbf{v})\,\mathbf{1} - 2\eta\,(\mathbf{v} \otimes \nabla)^{\mathrm{Sym}} \tag{2.14}$$

with the thermal conductivity λ, the volume and the shear viscosities η_{Vol} and η, respectively, which all are positive due to the second law of thermodynamics.

The heat conduction equation (2.7) alone cannot describe thermal processes, as the temporal change of pressure (or density), the convective change related to the velocity field, and viscous dissipation also affect the evolution of the temperature field. Therefore, the balance equations of mass and linear momentum

$$\dot{\varrho} + \varrho \nabla \cdot \mathbf{v} = 0, \tag{2.15}$$

$$\varrho \dot{\mathbf{v}} = -\nabla p - \nabla \cdot \mathbf{\Pi} + \varrho \mathbf{g} \tag{2.16}$$

must be coupled to the heat conduction equation, where $\varrho\mathbf{g}$ represents the volumetric force field, which, for instance, originates from the gravitational field. The equations (2.7), (2.13), (2.14), (2.15) and (2.16) form a closed system, so it can be solved with appropriate initial and boundary conditions.

2.2. **Thermal equilibration model near the critical point.** Let us now focus on the microgravity experiments conducted during the SpaceLab D2 mission [15]. Due to microgravity circumstances, the volumetric force field is negligible, *i.e.,* $\varrho\mathbf{g} = \mathbf{0}$. Following [13], fluid flow can be neglected (*i.e.,* $\mathbf{v} = \mathbf{0}$) when the fast initial acoustic propagation of the disturbances is out of scope. As a consequence, the material time derivative reduces to the partial time derivative. Correspondingly, the Navier–Stokes equation (2.16) and the heat conduction equation (2.7) reduce to

$$\nabla p = 0, \tag{2.17}$$

$$\varrho c_p \frac{\partial T}{\partial t} = -\nabla \cdot \mathbf{J}_Q + T\beta_p \frac{\mathrm{d}p}{\mathrm{d}t}. \tag{2.18}$$

In light of (2.17), pressure is homogeneous during the entire process; however, it remains time dependent and can play an important role in the dynamics of the temperature field, as shown by (2.18). Let us remark here that (2.17) is already built into (2.18), since instead of $\frac{\partial p}{\partial t}$ we have written $\frac{\mathrm{d}p}{\mathrm{d}t}$. Therefore, an additional dynamical equation is required to characterize the process. Since the tank is closed during the experiment, the mass of the filled fluid remains unchanged. Neglecting the thermal expansion of the walls and applying the thermal equation of state $\varrho(T, p)$ we obtain

$$0 = \frac{\mathrm{d}m}{\mathrm{d}t} = \frac{\mathrm{d}}{\mathrm{d}t}\int\limits_{\mathcal{V}} \varrho \mathrm{d}V = \int\limits_{\mathcal{V}} \frac{\partial \varrho}{\partial t}\mathrm{d}V = \int\limits_{\mathcal{V}} \left(-\varrho\beta_p \frac{\partial T}{\partial t} + \varrho\chi_T \frac{\mathrm{d}p}{\mathrm{d}t}\right)\mathrm{d}V. \tag{2.19}$$

Due to the homogeneity of the pressure the required dynamical equation can be formulated as

$$\frac{\mathrm{d}p}{\mathrm{d}t} = \frac{\int\limits_{\mathcal{V}} \varrho \beta_p \frac{\partial T}{\partial t} \mathrm{d}V}{\int\limits_{\mathcal{V}} \varrho \chi_T \mathrm{d}V}. \tag{2.20}$$

2.3. **Thermal processes on the time scale of the heat pulse.** The heat pulse excitation achieved by electric heating can be formulated as a time-dependent boundary condition

$$\mathbf{J}_Q \cdot \mathbf{n}\big|_{\partial\mathcal{V}} = \begin{cases} \frac{\overset{*}{Q}}{A_\mathrm{s}}, & \text{if } 0 \le t \le t_\mathrm{p}, \\ 0, & \text{otherwise,} \end{cases} \tag{2.21}$$

where $\overset{*}{Q}$ represents the heating power and A_s denotes the area of the heated surface, *i.e.,* the outer surface of the spherical tank. Although spherical geometry was used in the experiments [15], our goal is to study the material behavior in the simplest possible way, so we transform spherical coordinates into Cartesian coordinates. Therefore, let us suppose a pipe with length X, which has the same volume as the spherical tank, *i.e.,* $\frac{4\pi}{3} R_\mathrm{in}^3 = AX$, with the inner radius R_in of the spherical tank and the cross section of the pipe A. In order to effectively perform the analysis in one spatial dimension, the diameter of the pipe must be negligible compared to its length, *i.e.,* $\sqrt{A} \ll X$ must hold; furthermore, all surfaces of the tube must be adiabatically insulated, except for one base circle for the duration of the heat pulse. Accordingly, the only essential direction – the axial coordinate of the pipe – is denoted by x. We do not want to modify the duration of the heat pulse and the applied heating power, *i.e.,* heat $\overset{*}{Q} t_\mathrm{p}$ is kept constant, therefore, the boundary conditions for this problem are prescribed as

$$J_Q(t, x=0) = \begin{cases} \frac{\overset{*}{Q}}{A}, & \text{if } 0 \le t \le t_\mathrm{p}, \\ 0, & \text{otherwise,} \end{cases} \qquad J_Q(t, x=X) = 0. \tag{2.22}$$

Furthermore, let us now restrict ourselves to a linear analysis in accordance with the finding of [15]. Thus, let us introduce the new variables, *i.e.,* deviation from the initial equilibrium temperature and pressure $\hat{T}(t,x) = T(t,x) - T^0$ and $\hat{p}(t) = p(t) - p^0$. Substituting (2.13) into (2.18) and linearizing it together with (2.20), we obtain the system of linearized equations

$$\varrho^0 c_p^0 \frac{\partial \hat{T}}{\partial t} = \lambda^0 \frac{\partial^2 \hat{T}}{\partial x^2} + T^0 \beta_p^0 \frac{\mathrm{d}\hat{p}}{\mathrm{d}t}, \tag{2.23}$$

$$\frac{\mathrm{d}\hat{p}}{\mathrm{d}t} = \frac{\varrho^0}{\gamma^0} \beta_p^0 \left(a_s^0\right)^2 \frac{1}{X} \int\limits_0^X \frac{\partial \hat{T}}{\partial t} \mathrm{d}x, \tag{2.24}$$

with ^{0} denoting the values of thermophysical parameters in the initial state $\left(T^0, p^0\right)$, for instance, $\varrho^0 = \varrho\left(T^0, p^0\right)$. Introducing the dimensionless time and space variables

$\tau := {}^{t}/_{t_\mathrm{p}}$ and $\xi = {}^{x}/_{X}$, equations (2.23) and (2.24) can be transformed into the form

$$\frac{\partial \hat{T}}{\partial \tau} = \frac{t_\mathrm{p}}{{}^{X^2}/_{\alpha^0}} \frac{\partial^2 \hat{T}}{\partial \xi^2} + \frac{T^0 \beta_p^0}{\varrho^0 c_p^0} \frac{\mathrm{d}\hat{p}}{\mathrm{d}\tau}, \tag{2.25}$$

$$\frac{\mathrm{d}\hat{p}}{\mathrm{d}\tau} = \frac{\varrho^0}{\gamma^0} \beta_p^0 \left(a_s^0\right)^2 \int_0^1 \frac{\partial \hat{T}}{\partial \tau} \mathrm{d}\xi. \tag{2.26}$$

Via $\gamma^0 = \frac{c_p^0}{c_v^0}$ and utilizing the constancy of the parameters, (2.26) can be rewritten as

$$\frac{\mathrm{d}\hat{p}}{\mathrm{d}\tau} = \frac{\varrho^0}{\gamma^0} \beta_p^0 \left(a_s^0\right)^2 \int_0^1 \frac{\partial \hat{T}}{\partial \tau} \mathrm{d}\xi = \frac{\beta_p^0 \left(a_s^0\right)^2}{c_p^0} \int_0^1 \varrho^0 c_v^0 \frac{\partial \hat{T}}{\partial \tau} \mathrm{d}\xi. \tag{2.27}$$

Exploiting the linearized version of the relation $\mathrm{d}u = c_v \mathrm{d}T - \frac{1}{\varrho^2}\left(T\frac{\beta_p}{\chi_T} - p\right)\mathrm{d}\varrho$ (with u denoting the specific internal energy), the above integral can be further simplified, *i.e.,*

$$\begin{aligned} \frac{\mathrm{d}\hat{p}}{\mathrm{d}\tau} &= \frac{\beta_p^0 \left(a_s^0\right)^2}{c_p^0} \int_0^1 \left(\varrho^0 \frac{\partial \hat{u}}{\partial \tau} + \frac{1}{\varrho^0} \left(T^0 \frac{\beta_p^0}{\chi_T^0} - p^0 \right) \frac{\partial \hat{\varrho}}{\partial \tau} \right) \mathrm{d}\xi \\ &= \frac{\beta_p^0 \left(a_s^0\right)^2}{c_p^0} \left(\frac{\mathrm{d}}{\mathrm{d}\tau} \int_0^1 \varrho^0 \hat{u} \mathrm{d}\xi + \frac{1}{\varrho^0} \left(T^0 \frac{\beta_p^0}{\chi_T^0} - p^0 \right) \underbrace{\int_0^1 \frac{\partial \hat{\varrho}}{\partial \tau} \mathrm{d}\xi}_{\overset{(2.19)}{=} 0} \right) = \frac{\beta_p^0 \left(a_s^0\right)^2}{c_p^0} \frac{1}{X} \frac{\mathrm{d}\hat{U}_A}{\mathrm{d}\tau}, \end{aligned} \tag{2.28}$$

with the cross-section-specific internal energy of the fluid $\hat{U}_A = \int_0^X \frac{\partial \hat{\varrho}}{\partial \tau} \mathrm{d}x$. Since volume change of the tank is zero, the first law of thermodynamics for the whole system reads

$$\frac{\mathrm{d}U}{\mathrm{d}t} = \overset{*}{Q}, \tag{2.29}$$

and if the heat capacity of the pipe wall is neglected, then

$$\frac{\mathrm{d}\hat{U}_A}{\mathrm{d}\tau} = t_\mathrm{p} \frac{\overset{*}{Q}}{A}. \tag{2.30}$$

Therefore the pressure change in the fluid can be given as

$$\frac{\mathrm{d}\hat{p}}{\mathrm{d}\tau} = \frac{\beta_p^0 \left(a_s^0\right)^2}{c_p^0} \frac{t_\mathrm{p}}{X} \frac{\overset{*}{Q}}{A}. \tag{2.31}$$

This relationship highlights that in the linear approximation, if the heating power is constant, the pressure increases linearly. Furthermore, after the heat pulse, *i.e.,* when $\overset{*}{Q} = 0$, then the pressure remains constant. The pressure after the heat pulse

is obtained via integration of (2.31) over the pulse duration t_p, *i.e.,*

$$\hat{p}\left(t_\mathrm{p}\right) = \frac{\beta_p^0 \left(a_s^0\right)^2}{c_p^0} \frac{t_\mathrm{p}}{X} \frac{\overset{*}{Q}}{A}. \tag{2.32}$$

In the first term on the r.h.s. of (2.25) the ratio of the pulse duration and the diffusion time scale $t_\mathrm{d} = {X^2}/{\alpha^0}$ appears. Since $t_\mathrm{p} \ll t_\mathrm{d}$, in the beginning of the process (*i.e.,* on the fast time scale) ${t_\mathrm{p}}/{t_\mathrm{d}} \to 0$, hence (2.25) reduces to

$$\frac{\partial \hat{T}}{\partial \tau} = \frac{T^0 \beta_p^0}{\varrho^0 c_p^0} \frac{\mathrm{d}\hat{p}}{\mathrm{d}\tau}. \tag{2.33}$$

Let us remark that the spatial derivative on the fast time scale disappears, and hence in the bulk fluid (*i.e.,* outside the thin thermal boundary layer) the governing equation effectively reduces to a spatially uniform energy balance equation under a homogeneous initial condition. Consequently, the resulting ordinary differential equation (2.33) describes the evolution of a perfectly homogeneous bulk temperature, consistent with the observed (nearly) uniform temperature rise during the heat pulse. Integrating (2.33) yields the temperature outside the boundary layer after the heat pulse:

$$\hat{T}\left(t_\mathrm{p}, x\right) = \frac{T^0}{\varrho^0} \left(\frac{\beta_p^0 a_s^0}{c_p^0}\right)^2 \frac{t_\mathrm{p}}{X} \frac{\overset{*}{Q}}{A}. \tag{2.34}$$

Let us note here that substituting (2.31) into (2.23) yields the heat conduction equation

$$\frac{\partial \hat{T}}{\partial t} = \alpha^0 \frac{\partial^2 \hat{T}}{\partial \xi^2} + \frac{T^0}{\varrho^0} \left(\frac{\beta_p^0 a_s^0}{c_p^0}\right)^2 \frac{1}{X} \frac{\overset{*}{Q}}{A}, \tag{2.35}$$

where the last term represents a homogeneous volumetric heat source. However, this equation is limited by the assumed linearity and applied boundary conditions.

Let us observe that in the linear case the pressure and the temperature changes depend only on the geometry, heating power and the initial state, which determine the values of the emerging combinations of material properties. In (2.31), exactly the nondimensional Grüneisen parameter

$$\frac{1}{\varrho} \left.\frac{\partial p}{\partial u}\right|_\varrho = \frac{\beta_p a_s^2}{c_p} \tag{2.36}$$

appears, characterizing the isochoric pressure change caused by the change of specific internal energy, while in (2.33)

$$\left.\frac{\partial T}{\partial p}\right|_s = \frac{T}{\varrho} \frac{\beta_p}{c_p} \tag{2.37}$$

emerges, describing the isentropic temperature change caused by the pressure change. However, the dynamics of the temperature on the fast time scale is governed by the product of the previous two parameters [c.f. (2.34)]. Figure 3 presents the behavior of the parameters governing the dynamics for carbon dioxide near the liquid-vapor

critical point. The Grüneisen parameter, similarly to the isentropic speed of sound and thermal diffusivity, has local minima in the vicinity of the critical point. Note that the parameter $\frac{T}{\varrho}\left(\frac{\beta_p^0 a_s^0}{c_p^0}\right)^2$ has an inflection point around the critical point and has a steep slope in this region. Accordingly, processes initiated from the same initial pressure but slightly different initial temperatures can differ greatly even in the linear case, and consequently, the temperature rise during the heat pulse can also vary intensely.

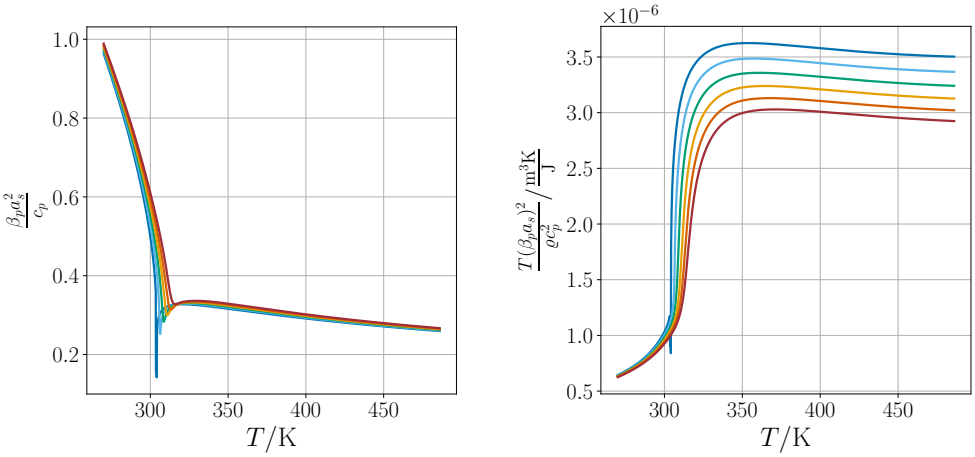

Figure 3. Temperature dependence of the parameters governing the piston effect for carbon dioxide along the isobaric lines $\approx 1p_\mathrm{c}$, $1.05p_\mathrm{c}$, $1.1p_\mathrm{c}$, $1.15p_\mathrm{c}$, $1.2p_\mathrm{c}$ and $1.25p_\mathrm{c}$ (from dark blue to red, respectively).

Finally, since the system is adiabatically insulated (except for the duration of the heat pulse) and isochoric, the temperature after homogenization can be calculated by the formula

$$\hat{T}(\infty, x) = \frac{1}{\varrho^0 c_v^0} \frac{t_\mathrm{p}}{X} \frac{\overset{*}{Q}}{A}. \tag{2.38}$$

The parameter $\frac{1}{\varrho^0 c_v^0}$ specifies the temperature change during the entire process. Its temperature dependence for carbon dioxide is presented in Figure 4.

3. An iterative numerical solution method

Although the temperature equilibration model can be simplified using linearization, heat pulse and adiabatic boundaries, for cases involving arbitrary boundary conditions and nonlinear extensions we propose a finite-difference-based approach to solve the coupled system of the pressure-corrected heat conduction equation (2.18), the pressure evolution equation (2.20), and Fourier's law (2.13).

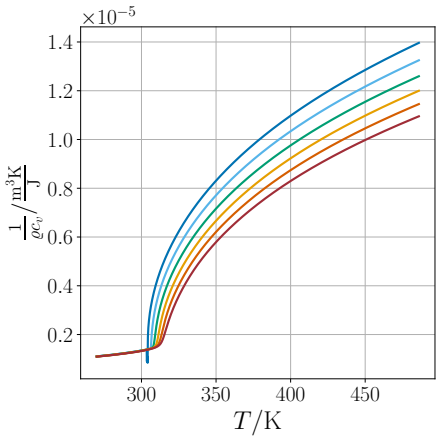

Figure 4. Temperature dependence of the parameters $\frac{1}{\varrho c_v}$ of carbon dioxide along the isobaric lines $\approx 1p_\mathrm{c}$, $1.05p_\mathrm{c}$, $1.1p_\mathrm{c}$, $1.15p_\mathrm{c}$, $1.2p_\mathrm{c}$ and $1.25p_\mathrm{c}$ (from dark blue to red, respectively).

The examined time interval is divided into equally spaced discrete time instants $t^j = j\Delta t,\ j = 0, 1, 2, \ldots$ with time step Δt, while spatial discretization is carried out on a staggered grid using equidistant cells. Temperature, as a bulk property, is located at the cell centers, while heat current density – representing inflow and outflow – is placed at the cell edges [26]. Since heat current density is prescribed at the boundaries, the one-dimensional domain $[0, X]$ can be divided into N cells with a size of $\Delta x = \frac{X}{N}$, hence $x_n = n\Delta x,\ n = 0, \ldots, N$. Accordingly, the spatial index of the heat current density is denoted via integers, while half indices are applied for the temperature, *i.e.,*

$$T\left(t^j, x_{n+1/2}\right) = T^j_{n+1/2} \qquad \text{and} \qquad J_Q\left(t^j, x_n\right) = (J_Q)^j_n\,. \tag{3.1}$$

The explicit Euler method is applied for time integration, whose stability is ensured via the choice of the time step. The stability condition of the classical heat conduction equation is $\Delta t \leq \frac{\Delta x^2}{2\alpha^0}$, which is considerably larger than t_p near the critical point. Therefore, for an appropriate resolution of the heat pulse the time step is chosen as

$$\Delta t = \min\left(\frac{\Delta x^2}{2\alpha^0}, \frac{t_\mathrm{p}}{10}\right). \tag{3.2}$$

Let us observe that both (2.18) and (2.20) contain the time derivatives of the temperature as well as of the pressure. A simple way to solve these coupled equations is to apply an iterative procedure. Correspondingly, within a single time step, first the temperature values $T^{j+1(k=0)}_{n+\frac{1}{2}}$ are determined from (2.18) without the pressure correction term. Then substituting these new values into (2.20), an estimate for the pressure $p^{j+1(k=1)}$ is determined. Subsequently, the determined pressure is substituted into (2.18), which now includes the pressure correction term and thus allows

computation of the corrected temperature values $T_{n+\frac{1}{2}}^{j+1(k=1)}$, which can be substituted into (2.20). This process continues until the difference of the temperature and pressure values between two iteration steps falls within the appropriately prescribed errors ε_T and ε_p. Thereafter, heat current density is determined from the discrete version of (2.13). The above-described iterative procedure is illustrated in Figure 5.

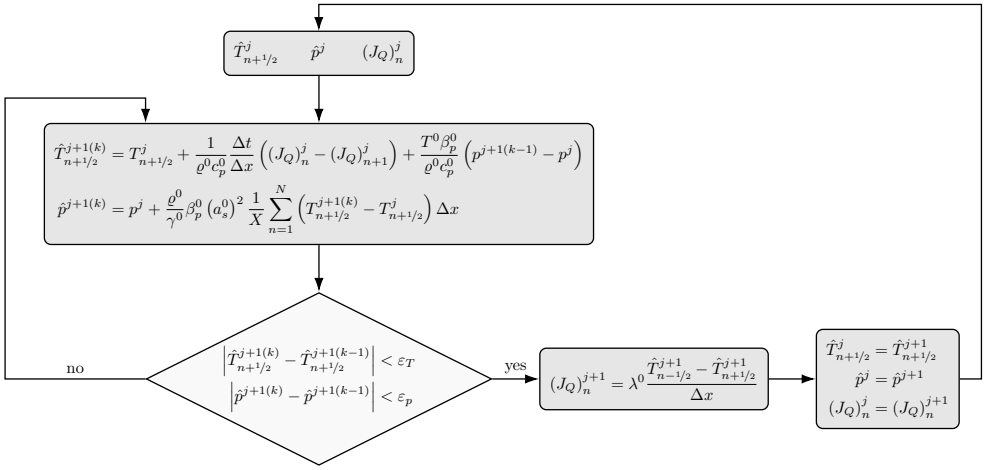

Figure 5. The iterative procedure for time integration of the governing equations

Let us note that equations (2.18), (2.20) and (2.13) are obtained neglecting the flow processes, but at this level, no linearization was applied. Therefore, the numerical scheme presented above is also applicable to investigation of material nonlinearities. Then, before the time-integration block the required material properties must be evaluated and slightly modified equations must be used for the time integration.

3.1. **Demonstration of the numerical solution.** Although sulfur hexafluoride was used in the spaceexperiment [15], carbon dioxide is used for numerical purposes. The reason for this is that high-precision, closed-form equations of state for carbon dioxide are available, which provide advantages in the planned numerical computation of the nonlinear processes. In this work, the Span–Wagner equation of state is applied, which condenses all thermostatic properties of carbon dioxide into a free energy function [17]. Thermal conductivity of the fluid is calculated using the reference correlation given by [18].

For all computations the parameters

$$R_{\text{in}} = 9.6 \text{ mm}, \qquad X = 100 \text{ mm}, \qquad \overset{*}{Q} = 3.85 \text{ mW}, \qquad t_{\text{p}} = 10 \text{ s} \tag{3.3}$$

and 100 cells along the x axis are applied, which, according to [27], provides adequate resolution for the investigation of the piston effect. All cases are computed for the duration of the diffusion time scale determined by the initial condition.

For the initial condition we have chosen $T^0 = 305$ K and $p^0 = 7.38$ MPa, accordingly, the governing parameters are $\frac{\beta_p^0 \left(a_s^0\right)^2}{c_p^0} = 0.288$, $\frac{T^0}{\varrho^0}\left(\frac{\beta_p^0 a_s^0}{c_p^0}\right)^2 = 2.32 \cdot 10^{-6}\ \frac{\mathrm{m^3K}}{\mathrm{J}}$, $\frac{1}{\varrho^0 c_v^0} = 2.57 \cdot 10^{-6}\ \frac{\mathrm{m^3K}}{\mathrm{J}}$ and $t_\mathrm{d} = 678208$ s. Table 1 presents the comparison of results obtained via the analytical formulas (2.32), (2.34) and (2.38) and via numerical simulation. The results obtained with both methods are convincing. Evolution of temperature distribution during the heat pulse is presented in Figure 6. The thermal boundary layer formed near the heated surface and the homogeneous temperature increase of the bulk fluid are clearly observed. Figure 7 shows how temperature distribution evolves after the heat pulse on the slow time scale, *i.e.,* during diffusion.

$\frac{T(t_\mathrm{p},X)-T^0}{\mathrm{K}}$		$\frac{T(\infty,x)-T^0}{\mathrm{K}}$		$\frac{p(t_\mathrm{p})-p^0}{\mathrm{Pa}}$	
analytical	numerical	analytical	numerical	analytical	numerical
0.0241	0.0241	0.0267	0.0267	2992.0	2991.4

Table 1. Comparison of analytical and numerical outcomes

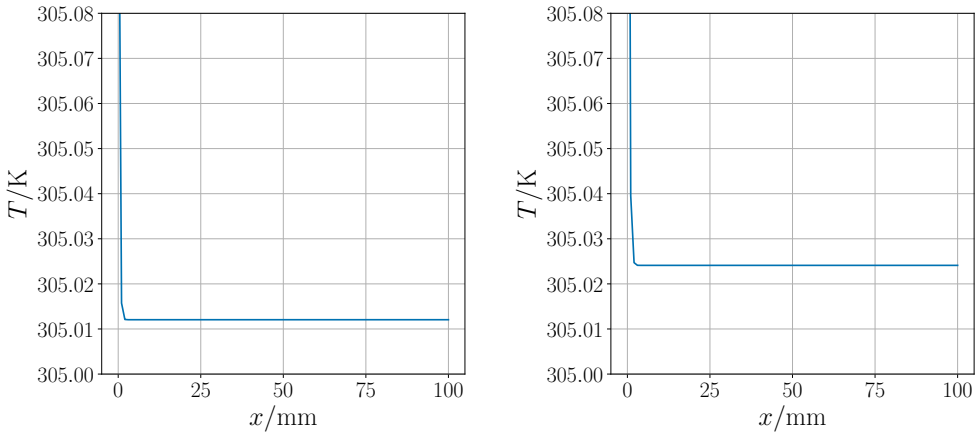

Figure 6. Temperature distribution during the heat pulse at the time instant $t = \frac{1}{2}t_\mathrm{p}$ (*left*) and at the time instant $t = t_\mathrm{p}$ (*right*)

4. Influence of initial conditions on the piston effect

Near the critical point, the governing parameters of the piston effect, similarly to the thermophysical properties, exhibit intense state dependence, as presented in Figures 3 and 4. Due to the linearization process presented above, through these governing parameters the emerging process depends on the initial state. Accordingly, in the vicinity of the critical point, relevant deviations in the solution are expected even in the linear case. In this section the sensitivity to the initial state is analyzed.

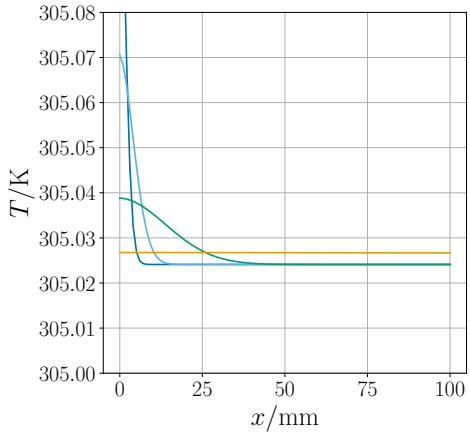

Figure 7. Temperature distribution on the diffusion time scale at the time instants $t = \frac{1}{5000}t_\mathrm{d}$, $\frac{1}{1000}t_\mathrm{d}$, $\frac{1}{100}t_\mathrm{d}$ and t_d (from dark blue to red, respectively)

4.1. **Sensitivity to initial temperature at constant initial pressure.** First, the influence of the initial temperature dependence is investigated at an unchanged initial pressure. Simulations are performed for initial temperatures $T^0 = 305$ K, 310 K, 315 K, 320 K and 325 K, while maintaining a constant initial pressure of $p^0 = 7.38$ MPa.

Figure 8 illustrates the pressure increase during the heat pulse and the initial values of its governing parameter. It can be seen that pressure rise during the process starting from the initial condition of 305 K differs significantly, whereas processes starting from the other investigated initial temperatures are nearly indistinguishable.

Similarly, Figure 9 presents the time evolution of temperature at the right boundary ($x = X$) during the heat pulse and the initial values of its governing parameter. The process starting from the initial condition of 305 K also differs significantly from the other cases.

In Figure 10, time evolution of temperature at the right boundary ($x = X$) on the diffusion time scale and initial values of the corresponding parameter are shown. The final temperature differences caused by the initial condition are obvious, as well as the harsh change of the diffusion time. The piston effect is best observed for the process starting from the initial temperature of 305 K, approximately 90 % of the temperature difference of the entire process occurs during the heat pulse, while the remaining 10 % only occurs during the incredibly long diffusion time. Moving away from the critical point, the length of the diffusion time scale normalizes and, in parallel, the temperature change occurring during the diffusion time scale accounts for an increasingly larger part of the temperature change during the entire process.

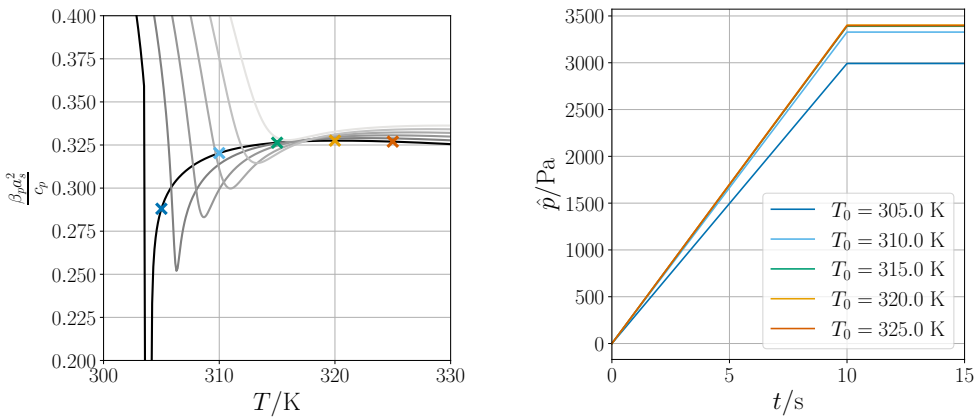

Figure 8. Influence of initial temperature on the parameter $\frac{\beta_p a_s^2}{c_p}$ (*left*) and on the time evolution of pressure increase during the heat pulse (*right*)

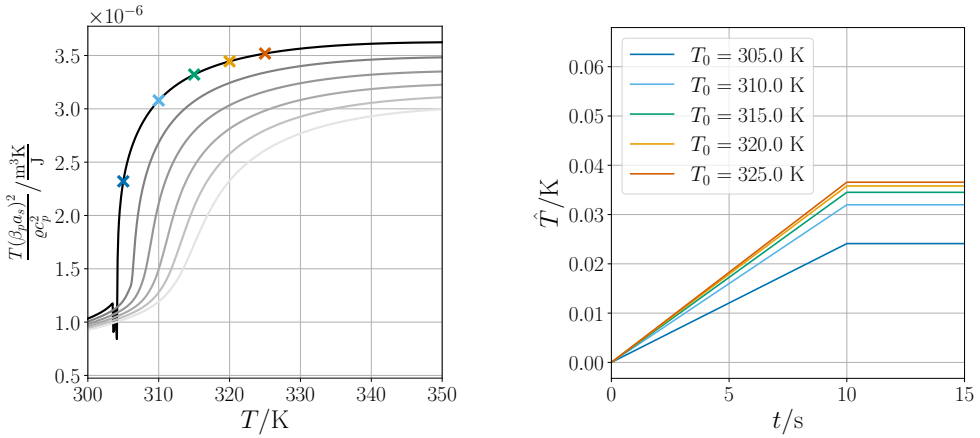

Figure 9. Influence of initial temperature on the parameter $\frac{T}{\varrho}\left(\frac{\beta_p a_s}{c_p}\right)^2$ (*left*) and on the time evolution of temperature increase at the spatial coordinate $x = X$ during the heat pulse (*right*)

4.2. **Sensitivity to initial pressure at constant initial temperature.** The influence of the initial pressure dependence is investigated at a constant initial temperature. Simulations are performed for initial pressures $p^0 = 7.38$ MPa, 7.48 MPa, 7.58 MPa, 7.68 MPa and 7.78 MPa, while maintaining a constant initial temperature of $T^0 = 305$ K. The results are presented in the same arrangement as before.

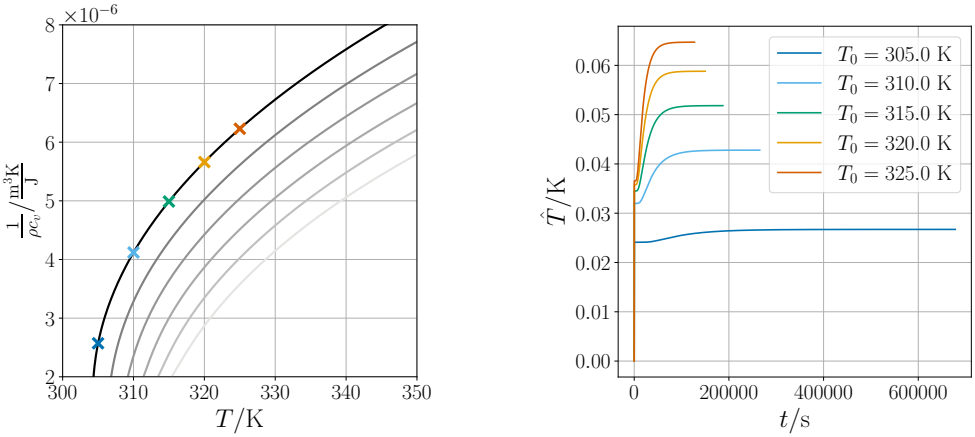

Figure 10. Influence of initial temperature on the parameter $\frac{1}{\varrho c_v}$ (*left*) and on the time evolution of temperature increase at the spatial coordinate $x = X$ on the diffusion time scale (*right*)

While in the case of increasing initial temperature, tendentious pressure and temperature increases during the heat pulse emerge, the opposite case is more hectic. The reason for this is that the governing parameters can take the same value at the same temperature but different pressures, so isobaric values of these parameters can intersect. Pressure rise and temperature rise during the heat pulse and the corresponding governing parameters are shown in Figures 11 and 12, respectively.

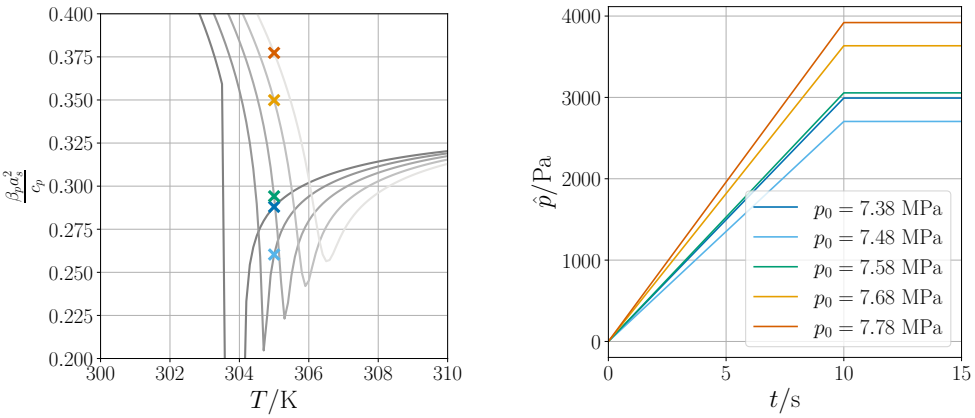

Figure 11. Influence of initial pressure on the parameter $\frac{\beta_p a_s^2}{c_p}$ (*left*) and on the time evolution of pressure increase during the heat pulse (*right*)

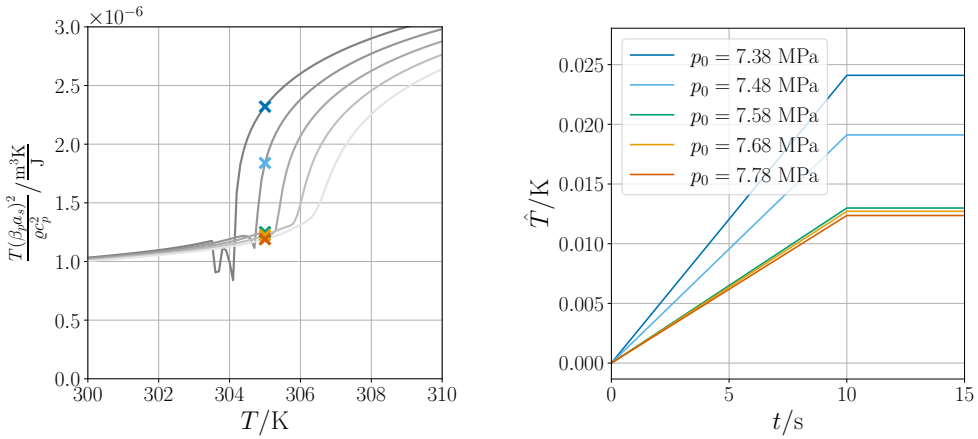

Figure 12. Influence of initial pressure on the parameter $\frac{T}{\varrho}\left(\frac{\beta_p a_s}{c_p}\right)^2$ (*left*) and on the time evolution of temperature increase at the spatial coordinate $x = X$ during the heat pulse (*right*)

Time evolution of temperature at the right boundary ($x = X$) on the diffusion time scale and initial values of the corresponding parameter are shown in Figure 13. The same digressive behavior can be observed and the piston effect can be well observed for all cases.

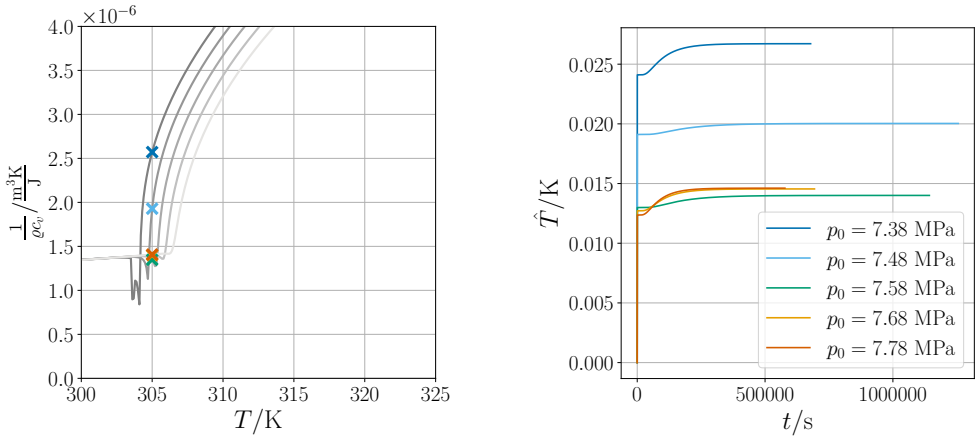

Figure 13. Influence of initial pressure on the parameter $\frac{1}{\varrho c_v}$ (*left*) and on the time evolution of temperature increase at the spatial coordinate $x = X$ on the diffusion time scale (*right*)

5. Discussion and outlook

The piston effect, a peculiar coupled thermo-mechanical phenomenon, emerges in the vicinity of the liquid–vapor critical point. Due to the exceptionally large value of the thermal expansion coefficient, pressure waves are generated in response to thermal excitation. These acoustic disturbances propagate rapidly through the fluid and lead to an apparently instantaneous temperature rise. In the heat pulse experiments the fast acoustic transients are suppressed by the long heating duration; nevertheless, the impact of the pressure on the temperature field remains essential and can be described by Boukari's thermal equilibration model, which approximation relies on a spatially homogeneous pressure field.

In this work, we have presented a detailed linear analysis of this model. On the short time scale of the heat pulse, diffusion is negligible, hence spatial derivatives vanish and the governing equations reduce to a system of ordinary differential equations. This simplified spatially homogeneous fast-time-scale limit enables an analytical approximation of the temperature and the pressure after the heat pulse. The resulting short-time-scale dynamics are controlled by two key parameters: one characterizing the isochoric pressure response to the internal-energy change (the Grüneisen parameter) and another describing the isentropic temperature change due to pressure variation. These parameters, similarly to conventional thermophysical properties, exhibit strong state dependence near the critical point. Consequently, even within the linear approximation, small variations in the initial temperature or pressure may lead to remarkable different responses. This sensitivity is confirmed by numerical simulations employing an explicit staggered-grid time-integration scheme with internal iteration. The proposed method can be straightforwardly extended to nonlinear problems in which material nonlinearities or more general boundary conditions are considered. For carbon dioxide, the influence of both the initial temperature and the initial pressure was demonstrated, and the numerical results show excellent agreement with the linear analytical predictions.

Although fluids above the critical point no longer exhibit a phase boundary, several thermophysical properties retain signatures of the liquid–vapor coexistence line in the form of extrema or inflection points. The loci of these anomalies in the supercritical region define the so-called Widom lines, which separate liquid-like and gas-like thermodynamic regimes. In contrast to the coexistence line, where many thermodynamic quantities exhibit finite jumps, each thermophysical property generally gives rise to its own Widom line. When a process crosses such a line, a qualitative change in the fluid's response may occur even without a phase transition. These features are inherited by the parameters governing the piston effect, suggesting that in the nonlinear regime further and more intricate behavior can be expected. Exploring such nonlinear thermo-mechanical interactions within the Widom region will form the basis of our future work.

6. Author contributions

K. Tóth: numerical computations, visualization, investigation of initial state dependence, manuscript text. M. Szücs: conceptualization, theoretical background, analytical calculations, supervision, manuscript text.

Acknowledgement. The research was supported by the Sustainable Development and Technologies National Programme of the Hungarian Academy of Sciences (FFT NP FTA) and by the Hungarian Scientific Research Fund under the Grant agreement NKKP STARTING24 149487.

References

[1] Akira Onuki. *Phase Transition Dynamics*. Cambridge University Press, 2002.

[2] Pierre Carlès. "A brief review of the thermophysical properties of supercritical fluids." *The Journal of Supercritical Fluids,* **53**(1), (2010), pp. 2–11. DOI: 10.1016/j.supflu.2010.02.017.

[3] Attila R. Imre, Axel Groniewsky, Gábor Györke, Adrienn Katona, and Dávid Velmovszki. "Anomalous properties of some fluids – with high relevance in energy engineering – in their pseudo-critical (Widom) region." *Periodica Polytechnica Chemical Engineering,* **63**(2), (2019), pp. 276–285. DOI: 10.3311/ppch.12905.

[4] Željko Knez, Elena Markočič, Maja Leitgeb, Mateja Primožič, M. Knez Hrnčič, and Mojca Škerget. "Industrial applications of supercritical fluids: A review." *Energy,* **77**, (2014), pp. 235–243. DOI: 10.1016/j.energy.2014.07.044.

[5] Mohammad Mizanur Rahman, Ji Dongxu, Nusrat Jahan, Massimo Salvatores, and Jiyun Zhao. "Design concepts of supercritical water-cooled reactor (SCWR) and nuclear marine vessel: A review." *Progress in Nuclear Energy,* **124**, (2020), p. 103320. DOI: 10.1016/j.pnucene.2020.103320.

[6] Pan Wu, Yanhao Ren, Min Feng, Jianqiang Shan, Yanping Huang, and Wen Yang. "A review of existing SuperCritical Water reactor concepts, safety analysis codes and safety characteristics." *Progress in Nuclear Energy,* **153**, (2022), p. 104409.

[7] Thomas Reinsch, Patrick Dobson, Hiroshi Asanuma, Ernst Huenges, Flavio Poletto, and Bernard Sanjuan. "Utilizing supercritical geothermal systems: a review of past ventures and ongoing research activities." *Geothermal Energy,* **5**(1), (2017), pp. 1–25. DOI: 10.1186/s40517-017-0075-y.

[8] Patrick Dobson, Hiroshi Asanuma, Ernst Huenges, Flavio Poletto, Thomas Reinsch, and Bernard Sanjuan. "Supercritical Geothermal Systems - A Review of Past Studies and Ongoing Research Activities." *42nd Workshop on Geothermal Reservoir Engineering.* Proceedings " 42nd Workshop on Geothermal Reservoir Engineering". Stanford, CA, United States, 2017.

[9] N. Longmire and D. T. Banuti. "Onset of heat transfer deterioration caused by pseudo-boiling in CO_2 laminar boundary layers." *International Journal of Heat and Mass Transfer,* **193**, (2022), p. 122957. DOI: 10.1016/j.ijheatmasstransfer.2022.122957.

[10] Bernard Zappoli. "Near-critical fluid hydrodynamics." *Comptes Rendus Mécanique,* **331**(10), (2003), pp. 713–726. DOI: 10.1016/j.crme.2003.05.001.

[11] Bernard Zappoli, Daniel Beysens, and Yves Garrabos. *Heat transfers and related effects in supercritical fluids.* Springer, 2015.

[12] B. Zappoli, D. Bailly, Y. Garrabos, B. Le Neindre, P. Guenoun, and D. Beysens. "Anomalous heat transport by the piston effect in supercritical fluids under zero gravity." *Physical Review A,* **41**(4),4 (1990), pp. 2264–2267. DOI: 10.1103/PhysRevA.41.2264.

[13] Hacène Boukari, J. N. Shaumeyer, Matthew E. Briggs, and Robert W. Gammon. "Critical speeding up in pure fluids." *Physical Review A,* **41**(4), (1990), p. 2260. DOI: 10.1103/PhysRevA.41.2260.

[14] Akira Onuki, Hong Hao, and Richard A Ferrell. "Fast adiabatic equilibration in a single-component fluid near the liquid-vapor critical point." *Physical Review A,* **41**(4), (1990), p. 2256. DOI: 10.1103/PhysRevA.41.2256.

[15] J. Straub, L. Eicher, and A. Haupt. "Dynamic temperature propagation in a pure fluid near its critical point observed under microgravity during the German Spacelab Mission D-2." *Physical Review E,* **51**(6), (1995), p. 5556. DOI: 10.1103/PhysRevE.51.5556.

[16] Kristóf Tóth. *A szuperkritikus dugattyúhatás kezdeti feltételektől való függésének vizsgálata (in Hungarian).* Student's Scientific Conference Thesis. 2025.

[17] Roland Span and Wolfgang Wagner. "A new equation of state for carbon dioxide covering the fluid region from the triple-point temperature to 1100 K at pressures up to 800 MPa." *Journal of physical and chemical reference data,* **25**(6), (1996), pp. 1509–1596. DOI: 10.1063/1.555991.

[18] Marcia L Huber, EA Sykioti, Marc J Assael, and Richard A Perkins. "Reference correlation of the thermal conductivity of carbon dioxide from the triple point to 1100 K and up to 200 MPa." *Journal of physical and chemical reference data,* **45**(1), (2016). DOI: https://doi.org/10.1063/1.4940892.

[19] Pierre Carlès. "Thermoacoustic waves near the liquid-vapor critical point." *Physics of Fluids,* **18**(12), (2006). DOI: 10.1063/1.2397577.

[20] Nusair Hasan and Bakhtier Farouk. "Thermoacoustic transport in supercritical fluids at near-critical and near-pseudo-critical states." *The Journal of Supercritical Fluids,* **68**, (2012), pp. 13–24. DOI: 10.1016/j.supflu.2012.04.007.

[21] Tamás Környey. *Hőátvitel (in Hungarian).* Műegyetemi Kiadó, 1999.

[22] Henning Struchtrup. *A Thermodynamic Introduction to Transport Phenomena.* Springer, 2024. DOI: 10.1007/978-3-031-61868-0.

[23] Ulrich Grigull. "Das Prinzip von Le Chatelier und Braun." *International Journal of Heat and Mass Transfer,* **7**(1), (1964), pp. 23–31.

[24] Tamás Matolcsi. *Ordinary Thermodynamics. Nonequilibrium Homogeneous Processes.* Budapest: Akadémiai Kiadó (Publishing House of the Hungarian Academy of Sciences), 2004.

[25] Adrian Bejan. *Advanced engineering thermodynamics.* John Wiley & Sons, 2016. DOI: 10.1002/9781119245964.

[26] Ágnes Rieth, Róbert Kovács, and Tamás Fülöp. "Implicit numerical schemes for generalized heat conduction equations." *International Journal of Heat and Mass*

Transfer, **126**, (2018), pp. 1177–1182. DOI: 10.1016/j.ijheatmasstransfer.2018.06.067.

[27] Donát M Takács, Tamás Fülöp, Róbert Kovács, and Mátyás Szücs. "The piston effect in supercritical fluids investigated via a reversible–irreversible vector field splitting-based explicit time integration scheme." *Physics of Fluids,* **37**(7), (2025). DOI: 10.1063/5.0271333.